Soft Matter

The effect of monomer polarizability on the stability and salt partitioning in model coacervates

Journal:	*Soft Matter*
Manuscript ID	SM-ART-05-2023-000706.R2
Article Type:	Paper
Date Submitted by the Author:	31-Jul-2023
Complete List of Authors:	Jedlinska, Zuzanna; University of Pennsylvania, Physics and Astronomy Riggleman, Robert; University of Pennsylvania, Chemical and Biomolecular Engineering

Soft Matter

ARTICLE TYPE

Cite this: DOI: 00.0000/xxxxxxxxxx

The effect of monomer polarizability on the stability and salt partitioning in model coacervates

Zuzanna M. Jedlinska,[a] Robert A. Riggleman*[b]

Received Date
Accepted Date

DOI: 00.0000/xxxxxxxxxx

Coacervation of charged polymer chains has been a topic of major interest in both polymer and biological sciences, as it is a subset of a phenomenon called liquid-liquid phase separation (LLPS). In this process the polymer-rich phase separates from the polymer-lean supernatant while still maintaining its liquid-like properties. LLPS has been shown to play a crucial role in cellular homeostasis by driving the formation of membraneless organelles. It also has the potential to be harnessed to aid in novel therapeutical applications. Recent studies have demonstrated that there is no one simple mechanism which drives LLPS, which is instead a result of the combined effect of electrostatic, dipolar, hydrophobic, and other weak interactions. Using coarse-grained polymer simulations we investigate the relatively unexplored effects of monomer polarizability and spatially varying dielectric constant on LLPS propensity, and these factors affect the properties of the resulting condensates. In order to produce spatial variations in the dielectric constant, all our simulations include explicit solvent and counterions. We demonstrate that polarizability has only a minor effect on the bulk behaviour of the condensates but plays a major role when ion partitioning and microstructure are considered. We observe that the major contribution comes from the nature of the neutral blocks as endowing them with an induced dipole changes their character from hydrophobic to hydrophilic. We hypothesize that the results of this work can aid in guiding future studies concerned with LLPS by providing a general framework and by highlighting important factors which influence LLPS.

1 Introduction

Solutions of charged polymers chains can undergo an electrostatics-driven phase separation called coacervation. If the oppositely charged monomers are placed on the same chain, the polymers are capable of creating the coacervate on their own, and the process is called self-coacervation. On the other hand, if multiple species carrying opposite charges associate together, the process is instead recognized as complex-coacervation. The driving forces that underlie coacervation are thought to play an important role in the formation membraneless organelles, and in biological contexts these polymer-rich phases are often referred to as condensates. Coacervation is also a type Liquid Liquid Phase Separation (LLPS) where the emergent polymer-rich phase still maintains its liquid-like properties[1,2]. Despite the large body of research regarding the properties of the condensates created through LLPS[3–5], the exact mechanism leading to their formation has yet to be fully understood. However, experimental results of the phase separation of synthetic polymers and disordered proteins have suggested that electrostatic, dipole, and hydrophobic interactions play an important role in this process[6–9].

LLPS is essential in biology where it leads to the sequestration of biomolecules within the cell, the formation of membraneless organelles, and chromatin condensation.[10–13]. When deregulated, intracellular LLPS can have detrimental consequences as the formation of pathological protein aggregates has been linked to the onset of neurodegenerative disease[14–16] and cancer[17,18]. In a pharmaceutical context, the phenomenon of LLPS has emerged as an important factor influencing the effectiveness of drug delivery in the case of substances with poor water solubility[19–21]. It has also been suggested that directly targeting and exploiting the intracellular LLPS can serve as a novel way to treat disease and to precisely deliver therapeutical agents which otherwise lack specific binding sites[22,23]. Thus, a complete understanding of the forces that drive condensation and coacervation is necessary not only for synthetic polymer materials but also for potential therapeutic applications.

One approach to understand LLPS and the formation of biomolecular condensates has been to study model and synthetic polymers that exhibit LLPS driven by similar thermodynamic forces. Coacervate-forming systems in particular have played an important role in our understanding of LLPS where enthalpic contributions, often due to polymer interactions with the solvent, and entropic forces, typically from the role of counterions in the

[a] Department of Physics and Astronomy, University of Pennsylvania, Philadelphia, USA.
[b] Department of Chemical and Biomolecular Engineering, University of Pennsylvania, Philadelphia, USA. E-mail: rrig@seas.upenn.edu

system, compete to drive LLPS[24–28]. A wide variety of models have been developed to study LLPS and specifically coacervation, and a variety of important factors have been examined, including the effects of solvent quality, addition of salt, and charge patterning[29–38].

The dependence of LLPS on particular sequence features, such as charge fraction and the charge pattern along the chain, has been studied extensively by theoryand simulation. Especially, "sequence charge decoration" and charge blockiness have been implied to play a significant role[39–41]. The propensity to undergo LLPS has also been correlated with the properties of a single chain[42]. The nature of water as the protein solvent and the proteins' dissolved ions has also prompted the authors to include the effect of these charged species on LLPS. In a recent field-theoretic study by[43] it has been found that electrolytic species can influence LLPS in a complex manner, hindering it at low concentrations, and enhancing at high salt concentrations, thus producing a re-entrant phase behaviour.

One factor that has not been explored in detail in coarse-grained models is the effect of spatial variations in the polarity of the system, which is known to affect a variety of thermodynamic factors including ion solvation and the effective interactions between species of dissimilar polarity[44,45]. Previous work has shown that, depending on the magnitude of the spatial variations in polarity (typically captured through a relative dielectric constant), substantial changes to equilibrium phase diagrams can emerge[46]. Monomer and solvent polarity has significant effects when performing detailed full-atom or fine-grained simulations, and it has also been shown[47] that polar explicit solvent models have subtle but important consequences when the bulk behaviour and stability of large biocondensates are considered. However, specifically isolating the role of polarity of the polymer monomers has not been considered.

Our study is motivated by theoretical and experimental results regarding the possible origins of biological LLPS, and intended to fill the gap in the understanding how monomer and solvent polarizability can drive this phenomenon. In this work we utilize coarse-grained simulations of polymer chains to investigate how monomer polarizability and the charge fraction of the sequence influence the stability of the coacervates, and how these factors affect the propensity to undergo LLPS. Our models are not intended to reproduce the behaviour of any specific polypeptide sequence. Instead, we aim to reproduce experimental observations using our minimal model in order to elucidate which interactions contribute to the occurrence of LLPS and what is the magnitude of their respective contributions. Thus, we focus only on simple sequences, namely, a charged diblock with two oppositely charged blocks, neutral homopolymers with and without polar monomers, and a triblock polymer with oppositely charged ends and a neutral midblock. There are multiple ways in which polarizability can be incorporated into the simulation, such as fluctuating charge and electronic continuum methods, and classical Drude oscillators[48–52]. To maintain the simplicity of the model, we utilize classical Drude oscillators as a proxy for molecular polarizability[53]. In this model, a small charged Drude particle is attached to the parent atom with the harmonic spring. It can later be integrated with other particles using classical equations of motion. The associated spring constant and the magnitude of the assigned charge are phenomenological parameters that can be parameterized to match experimental data. In fully atomistic simulations, when better resolution and more accurate polarizability model is desired, other, more computationally intensive methods should be used. For our purpose, however, the classical Drude oscillator model is sufficient, as our systems are already highly-coarse grained, and this method has the advantage of being computationally inexpensive and intuitive.

The outline of this paper is as follows. In Section 2 we provide the necessary background about the computational framework used, as well as the specific details about the set-up of the simulated systems. Subsequently, in Section 3 we present the results associated with the simulated systems. In Section 3.1 we begin by investigating the phase diagram of resulting from the use of different chain architectures and varying the polarizability of the monomers. Subsequently, in Section 3.3, we explore the effect of the length of the charged blocks on the phase behaviour of the triblock chains. Then, in Section 3.4, we analyze how the charge fraction and variations in polarizability of the blocks affect salt partitioning. Finally, in Section 3.5, we demonstrate how monomer polarizability can affect the microstructure developing in the polymer-rich phase. We conclude with a brief summary of the findings and a discussion of possible future research directions in Section 4.

2 Methods

2.1 Polymer Model and Theoretically Informed Langevin Dynamics (TILD)

The simulation framework employed in this work is called Theoretically Informed Langevin Dynamics (TILD), which is a hybrid particle/field method. In this approach, bonded interactions are computed using explicit particle coordinates while non-bonded interactions use a density-field representation. The density fields are generated through a particle-to-mesh scheme similar to those used in particle-to-mesh Ewald methods[54], with the density of each particle is interpolated between the discrete grid-points. The "smeared" densities are obtained by convolving the initial point-density of the particle with a unit Gaussian. The same scheme applies to charges, thus neither the density or charge are point-like in the TILD simulations, and the Gaussian smearing makes the models free of so-called ultraviolet divergences[38,55]. The choice of the smearing length, corresponding to the standard deviation of the Gaussian, can be used to adjust the effective size of the particle. During the simulation, each particle is acted on by the mean mass or charge density of the other particles. A schematic demonstrating the basics of the method is shown in Figure 1. For coarse-grained systems with relatively high particle densities, the TILD method is more efficient than standard molecular dynamics (MD) approaches by minimizing the use of explicit coordinates and thus the need for generation of computationally expensive neighbour-lists. In addition, the force calculations can be calculated efficiently in the Fourier space utilizing Fast Fourier Transform (FFT) libraries. The use of explicit coordinates cannot be

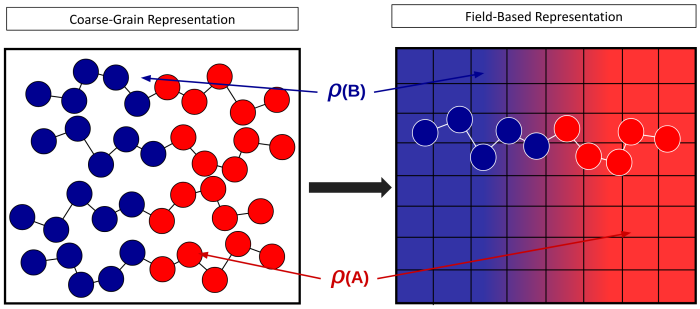

Figure 1 Schematic representations of the TILD approach. (Left): Coarse-grained polymer models, with monomers connected by bonds.; (Right) A field-based representations, where each monomer interacts with the mean density field generated by other monomers. Bonded interactions are handled using explicit coordinates. $\hat{\rho}(A)$ and $\hat{\rho}(B)$ correspond to the effective density of the given monomer type (A or B) at the discrete point.

avoided when bonded interactions are present, since these depend on inter-particle distances.

All simulations are performed using MATILDA.FT, our in-house GPU-accelerated software which available open-source on GitHub. A detailed discussion of the TILD method, the associated theoretical background, and the implementation details can be found in our previous manuscript[56], and the relationship between the TILD method and related field-theoretic approaches has recently been outlined[57,58].

We model polymers as discrete Gaussian chains[59] with monomers connected through harmonic bonds. The bonded potential is given by

$$\beta U_0 = \sum_{j}^{n} \sum_{s}^{N-1} \frac{3}{2b^2} |\mathbf{r}_{j,s} - \mathbf{r}_{j,s+1}|^2, \tag{1}$$

where b is statistical segment length, $\mathbf{r}$ is the position vector, j is used to index a particular chain, and s enumerates the monomers along the chains.

All simulations include an explicit polarizable solvent and non-polarizable counterions to allow us to capture the effects of spatially-varying dielectric constant and ion solvation effects, which are known to influence the behavior of polypeptide chains[60,61]. We model polarizability with classical Drude oscillators[62–64], see Figure 2 a). In this method, a small "Drude particle" is attached to the parent particle with a harmonic spring with an equilibrium separation of 0, and is assigned a partial charge $-\delta q_D$, while the parent particle gains an additional charge equal to $+\delta q_D$. Thus, the original charge in the system remains unchanged. The stiffness of the harmonic spring can be used to modulate molecular polarizability; a stiffer spring corresponds to a less polarizable molecule. Drude particles do not participate in any other interaction potentials, and they are assigned a unit mass so they can be integrated along with other particles using classical equations of motion. While this treatment of polarizability is computationally inexpensive, it does, however, come with limitations. Due to its classical nature, Drude oscillators are unable to capture quantum-mechanical effects, and in order to model real systems, the parameters used in the model need to be fitted to the experimental data. Since the charge gets assigned to a "Drude particle" this model is not adequate when spatial distribution of the charge around its parent particle is important. For the purpose of our study, we find this approach sufficient to represent the effect of polarizability and spatial variations in the dielectric constant.

The repulsive interactions between the monomers and the solvent are mediated through a Flory-Huggins potential, given by

$$\beta U_1 = \frac{\chi}{\rho_0} \int d\mathbf{r} \int d\mathbf{r}' \, \hat{\rho}_P(\mathbf{r}) \, u_G(|\mathbf{r} - \mathbf{r}'|) \, \hat{\rho}_S(\mathbf{r}'), \tag{2}$$

where the strength of the repulsion is set by the magnitude of the Flory-Huggins χ parameter. In Equation 2, $\hat{\rho}_P$, and $\hat{\rho}_S$, correspond to the density fields of the polymer monomers and the solvent, respectively. u_G is a unit Gaussian potential, $u_G(r) = (2\pi\sigma^2)^{-\mathbf{D}/2} e^{-r^2/2\sigma^2}$, $\mathbf{D}$ is the dimensionality of the system, and σ controls the range of the interactions. An additional excluded volume potential[65] penalizes the deviation from the average number density $\rho_0 = nN/V$ and is given by

$$\beta U_2 = \frac{\kappa}{2\rho_0} \int d\mathbf{r} \int d\mathbf{r}' \, [\hat{\rho}_+(\mathbf{r}) - \rho_0] \, u_G(\mathbf{r} - \mathbf{r}') \, [\hat{\rho}_+(\mathbf{r}') - \rho_0], \tag{3}$$

where $\rho_+(\mathbf{r})$ is sum of all species densities present in the system at discrete point $\mathbf{r}$ excluding Drude particles, which do not contribute to the number density.

Since the simulations consist of charged and polarizable molecules, charged species interact with their surrounding through the Coulomb potential. To calculate the electrostatic potential at a given point, $\phi(\mathbf{r})$, we numerically solve the Poisson equation,

$$\nabla^2 \phi(\mathbf{r}) = -4\pi l_B \check{\rho}_c(\mathbf{r}), \tag{4}$$

where l_B is the Bjerrum length and $\check{\rho}_c(\mathbf{r})$ is the Gaussian-smeared charge density, defined as $\check{\rho}_c(\mathbf{r}) = \sum_j q_j \, u_C(r - r_j)$ where $u_C(r) = (2\pi\sigma_C^2)^{-\mathbf{D}/2} \, e^{-r^2/2\sigma_C^2}$, and σ_C is the charge smearing length.

2.2 Simulation Details

For simplicity, we only focus on three simple polymer sequences, depicted in Figure 2 b): a charged diblock, neutral homopolymer, and a triblock polymer with charged blocks at each end and the neutral block in the center. All chains are net neutral, with the oppositely charged blocks always having equal lengths. Polymer chains have the total length of $N = 74$ for the case of a diblock, and $N = 75$ for the neutral homopolymer and the triblock. We only study homogeneous solutions, with only a single type of polymer chain present at a time, along with the solvent and ions.

Our systems are weakly compressible, with $\kappa = 3.5$, responsible for penalizing deviation from the mean number density, set to $\rho_0 = 3.0$ for all systems. Repulsive interactions between the monomers and the solvent are mediated through a Flory-Huggins χ parameter. This parameter is set to 0 for other interaction types, thus other species in the system interact only through excluded volume interaction (Equation 3). All dimensionless concentrations are reported in terms of C^*, where the densities are nondimensionalized by multiplying by $\frac{R_g^3}{N}$. Here, R_g is the the radius

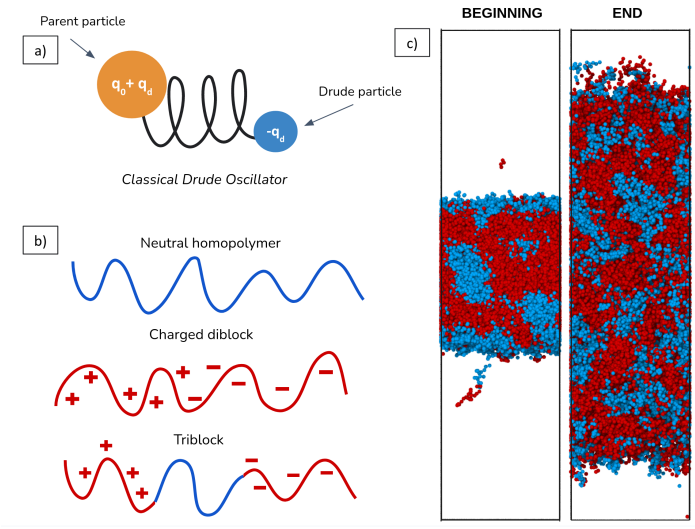

Figure 2 Schematic representations of different components of the simulations, and representative snapshots from the simulation: a) A cartoon representation of the classical Drude oscillator, with the parent particle, depicted in yellow, and the "Drude particle", depicted in blue, attached to it by a harmonic spring. b) Three simple chain sequences used in the simulations. Starting from the top: neutral homopolymer, charged diblock and a triblock polymer. c) Representative snapshots from the beginning "slab" configuration (left), and from the end of the simulation (right). Particles are rendered as spheres with radius equal to the Gaussian potential range, σ.

of gyration of the polymer chain given by $R_g = \sqrt{\frac{Nb^2}{6}}$. All length scales reported below are given in units of b. All systems with charged monomers involve explicit counterions, with one counterion per charged monomer. Optionally, varying amount of excess salt can also be present. All ions are modeled as univalent, non-polarizable spheres, with no distinction between counterions and salt ions.

Unless otherwise specified, simulations are performed in an orthogonal 3D box, with a square base and elongated along the z-axis with $\frac{z}{x}$ ratio ≥ 5. The shortest box dimensions are chosen to be $> 5R_g$ in order to avoid self-interactions of the chains and to minimize the influence of the finite-size effects. Since, in this work, we are only interested in the stability of the coacervates, and not their mechanism of formation, we start our simulations from a biased, "slab", configuration, depicted in Figure 2 c), with the polymer-rich phase already preformed in the middle of the box. At the beginning of the simulation, polymer chains are randomly distributed throughout the volume of the box, and subsequently pushed slowly towards its center by an external force. After the slab is formed, this additional force is removed, and the slab is allowed to expand and reach its equilibrium density. This method allows us to achieve better sampling in the region of interest, having a large ratio of the bulk phase as compared to the amount of interfacial area. This method has previously been implemented in[66,67] to study the stability of condensates in other coarse-grained models.

The values of parameters used in the simulations are summarized in the Table 1.

Table 1 List of parameters used in the simulations

Parameter	Value
N (chain length)	75 or 74
κ (compressibility)	3.5
ρ_0 (number density)	3.0
σ (Gaussian potential range)	1.0
σ_C (charge smearing length)	0.5
b (Statistical segment length)	1.0
l_b (Bjerrum length)	55.0
k_{bond} (bond spring constant)	1.0
k_{drude} (Drude oscillator spring constant)	2.5

3 Results

In this section we present the results obtained from simulations of different chain architectures with variable block polarizability. Our results are consistent with the previous work on polarizability[47,68,69], which suggests that including polarizability will have only a minor but noticeable effect on the bulk properties of the condensates. In line with that, we do not observe significant changes to the phase diagrams when polarizability is varied. However, our study has shown a novel effect which emerges from the explicit treatment of monomer polarizability and inclusion of explicit polar solvent. This approach creates spatially varying dielectric environment, which is an emergent property of the system itself. As we describe in more detail below, inclusion of these factors has a significant effect on ion partitioning and on the development of microstructure in the coacervates. We demonstrate that dielectric mismatch can provide another driving force towards microphase separation, while similarities in polarizability can enhance miscibility of distinct species in the system.

3.1 Monomer Polarizability

We begin by studying how monomer polarizability affects the phase diagram of coacervates as the magnitude of the Flory-Huggins χ-parameter between the solvent and monomers is varied. We only focus on three simple polymer architectures, depicted in Figure 2 b), which allows us to independently explore the behaviour of neutral, charged and mixed systems. As expected, in all cases the density in the condensed phase increases monotonically with increasing χ.

Next, we focus on the differences in the density of the coacervates introduced by variations in the polarity of the monomers. We start with the charged diblock, whose phase diagram is depicted in Figure 3 (top panel). We observe that at all corresponding values of χ, polarizable coacervates have higher density than their non-polarizable counterparts. In the case of coacervates created by neutral homopolymers, Figure 3 (middle panel), the trend in density is non-uniform. Below $\chi \sim 2.0$, non-polarizable coacervates have higher concentration. Above this value, the polarizable chains create denser condensates instead. Finally, the neutral and charged blocks are combined in a triblock architecture, Figure 3 (bottom panel), where we consider all four possible polarizability combinations. We observe that the main trend in the density is set by the character of the charged blocks, as there are two clearly separated, low- and high-density bands, corresponding to the non-polarizable and polarizable charged blocks, respectively.

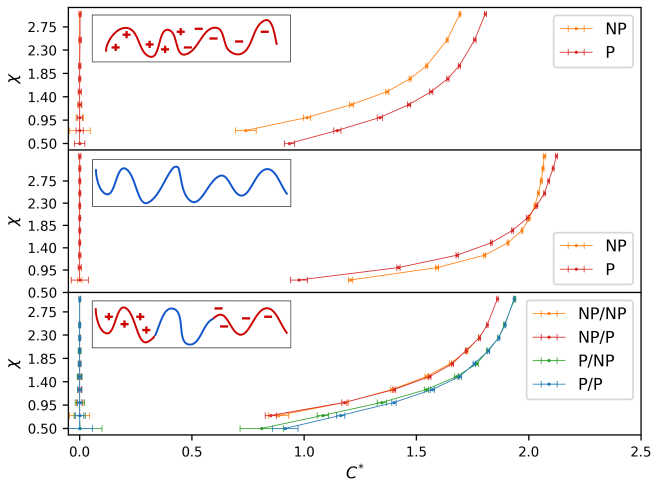

Figure 3 Phase diagrams of the coacervates created by the three different chain types used in our simulations as a function of the Flory χ parameter: the charged diblock (top), the neutral homopolymer (middle), and the triblock (bottom). In top and middle panels, the NP and P labels denote non-polarizable and polarizable molecules, respectively. In the bottom panel the first entry in the legend indicates the polarization condition of the charged end blocks, and the second indicates that for the uncharged midblock. Points corresponding to fully dissolved coacervates were omitted, and the reported concentrations of 0 correspond to concentrations too low to measure in our finite-sized simulation box.

The nature of the neutral block acts as a small perturbation added on top of this dominant effect and is visible only at low values of χ as the critical point is approached. At low values of χ, the combination of polarizable charged blocks with a polarizable neutral block reaches the highest concentration within the coacervate. This is in contrast to the coacervates created purely by neutral chains, which at the corresponding low χ values have higher density in the non-polarizable case.

The stability of condensates at the lowest value of χ studied (0.5) varied depending on the type of monomers and their polarizability. The coacervates including polarizable charged monomers (both diblock and triblock polymers) are stable at the lowest value of χ, whereas their non-polarizable counterparts dissolve. This suggests that the critical value of χ is lower for the chains with polarizable charged monomers, due to their enhanced attractive interactions. Neutral homopolymers do not form a polymer-rich phase at $\chi < 0.7$, due to the lack of the electrostatic attraction between the neutral species.

We explain the observed trends by noting that there are two main enthalpic contributions present in our systems. The bare electrostatic forces have the greatest effect, while the interactions between the dipoles contribute to a lesser extent. The electrostatic attraction between the oppositely charged monomers makes them pack more densely. However, it also draws the polar solvent molecules to the interior of the condensate. In contrast, neutral molecules display no such favorable electrostatic interactions.

Another enthalpic contribution to the energy are dipolar interactions between the polarizable-polarizable and polarizable-charged monomer pairs. These "coarse-grained van der Waals" are short ranged and attractive, and thus cause the polarizable particles to pack more densely. Thus, in the case of the charged condensates, the monomers and the solvent molecules can pack more closely and thus reach a higher density.

In the case of phase separation in the neutral systems, the trend in density is non-uniform. At low values of χ the solvent molecules are not effectively repelled by the monomers. When neutral monomers are polarizable and "hydrophilic", they preferentially draw the polar solvent into the polymer-rich phase, thus lowering overall density to maintain an average density of approximately ρ_0. At higher values of the χ, however, the solvent is expelled and polarizable monomers can pack more closely due to the interactions between their induced dipoles. When both neutral and charged monomers are combined, the final effect depends on their relative ratio. In the case of Figure 3 (bottom panel), the charged monomers dominate and thus set the main trend in the shape of the phase diagram. In addition, the polarizable-neutral block has a lower dielectric mismatch with polarizable-charged block, and this combination produces the condensate with the highest density at low values of χ.

3.2 Solvent polarity

Since all our simulations include explicit solvent, we investigate how the phase diagrams change with variations in the dielectric constant of the solvent. We focus only on the fully charged (diblock) and fully neutral (homopolymer) chains. We chose two different values of the effective dielectric constant of the solvent, ε_r, and perform a sweep in the χ-parameter space, see Figure 4. From the results obtained for the charged diblock (top panel), we observe that solvent polarity affects the non-polarizable and polarizable coacervates differently. Making the solvent more polar (increasing the value of ε_r) decreases the density of the non-polarizable coacervates. In contrast, the polarizable-charged coacervates have higher concentration in a more polar solvent. These differences in density diminish with the increasing χ.

A distinct behaviour is observed for the coacervates created by neutral homopolymers, Figure 4 (bottom). In this case, the polarity of the solvent has no effect on the density of the polarizable condensate but it affects the non-polarizable one. At low values of χ, the density of the non-polarizable coacervate is increased by a more polar solvent, and this effect diminishes as the magnitude of χ increases.

3.3 Charge fraction

In the following section, we focus on the effects of charge fraction in coacervates with different polarizability for the triblock polymer architecture shown schematically in Figure 2 b). We keep the total length of the chain constant at $N = 75$, and simultaneously vary the length, N_c, of the two charged blocks. The positive and negative terminal blocks always have the same lengths, thus the chains are net neutral. For simplicity, we also fix the charged blocks to be polarizable but still vary the character of the central neutral block.

As previously, we begin by incrementally increasing the repulsion strength, χ, between the monomers and the solvent and ob-

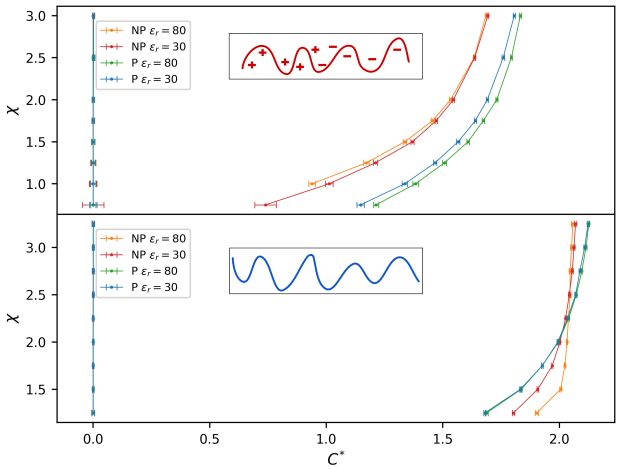

Figure 4 Effects of solvent polarity on the polymer concentration in the polymer-rich phase for the charged diblocks (top) and the neutral polymers (bottom). The NP and P labels denote non-polarizable and polarizable molecules, respectively, and the values of ε_r are the dielectric constants of bulk simulations of the pure solvent phase. Points corresponding to the fully dissolved coacervates were omitted, and the reported concentrations of 0 correspond to concentrations too low to measure in our finite-sized simulation box.

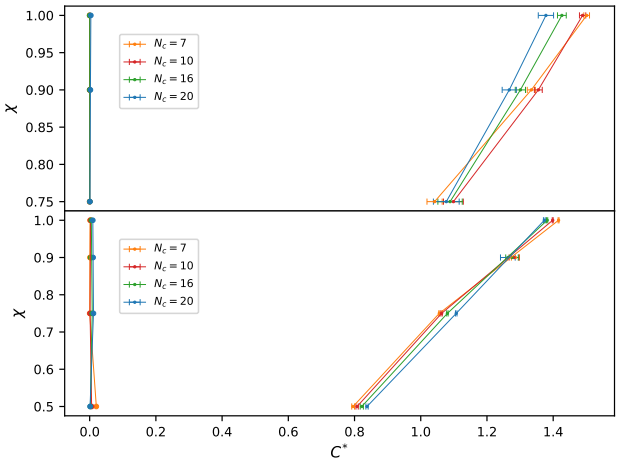

Figure 5 Effect of charge fraction on coacervates with different charge fractions, with non-polarizable (top) and polarizable (bottom) neutral blocks. In the polarizable case, below $\chi \approx 0.9$, the density of the coacervates increases with with the fraction of the charged molecules. Above this value this trend is reversed, and coacervates with lower charge fraction reach higher concentration. The value of χ where the trend reverses for the non-polarizable coacervates is lower.

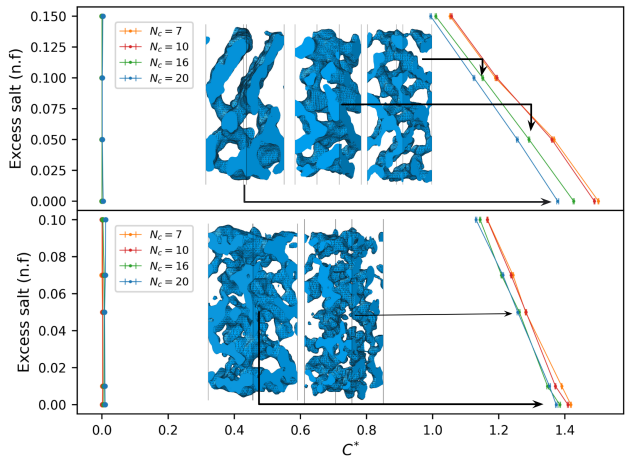

Figure 6 Response to excess salt of coacervates formed from triblock copolymers with different charge fractions. Insets depict the surface of charged domains of coacervates with $N_c = 16$. Non-polarizable neutral block (top) results in lamellar microstructure at no excess salt conditions, which becomes disordered as salt concentration increases. No microstructure develops for the case of polarizable neutral block (bottom) and the domains are poorly defined. n.f. stands for number fraction.

serve how the resulting phase diagram is affected by the fraction of charged monomers on the chain. Results are displayed in Figure 5. In both cases of the polarizable and non-polarizable midblocks, the phase diagram can be divided into two regions. Below $\chi \approx 0.9$, polarizable coacervates formed from chains with a higher charge fraction have higher concentration. Above this value of χ, the trend reverses, and the chains with a lower charge fraction result in the coacervates with higher density. The value of χ at which this transition occurs for the non-polarizable coacervates is lower. This effect is more pronounced in the case of non-polarizable neutral block (top panel) as compared to the chains where the central block is polarizable (bottom panel).

Subsequently, we fix the value of χ at 1.0 and introduce excess salt into the system to observe how the density and microstructure within the coacervates is affected by additional ions. We introduce the ions in a pair-wise manner, both carrying equal and opposite unit charges so that the system maintains charge neutrality. The results are shown in Figure 6. The insets depict the surfaces of the charged domains for the coacervates with $N_c = 16$, which we discuss in more detail below. As expected, the density of all coacervates decreases as the concentration of salt is increased. When the neutral block is non-polarizable (top) and no excess salt is present, a lamellar microstructure with residual defects develops. As more salt is introduced into the system, this microstructure becomes disordered. In contrast, no microstructure develops in the coacervates with polarizable neutral block and the charged domains are poorly ordered.

3.4 Salt partitioning

A novel aspect of our modeling approach is the potential for the emergence of spatial variations in the dielectric constant and thus ion solvation, which is expected to affect the partitioning of ions in our system. In this subsection, we focus on salt partitioning,

which refers to the way in which ions distribute themselves between the coacervate and the supernatant, and then within the different domains of the polymer-rich phase. We focus on the simulations described above as a function of N_c at a fixed value $\chi = 1.0$.

We begin by plotting the ratio of the ionic concentration within the coacervate to the concentration of ions in the supernatant. We monitor how this ratio of ion concentrations changes as a function of charge fraction and the polarizability of the neutral block. For simplicity, the charged blocks are always polarizable. The results are plotted in Figure 7. Beginning with the case of non-polarizable neutral block (Figure 7, middle panel) we observe that the concentration ratio scales proportionally to the charge fraction on the polymer chains, and the ratio is the highest for the coacervates with the largest charge fraction. As excess salt is introduced, the ratios monotonically increase for all values of excess salt considered here, independent of the charge fraction. On the other hand, in the case of polarizable neutral block (bottom panel), the trend is reversed. The relative concentration of ions within the coacervate is inversely proportional to the charge fraction. However, that the range over which the data is spread is much narrower. All concentration ratios for the polarizable neutral block are always above these corresponding to the non-polarizable counterparts. The concentration ratios in the bottom panel do not change appreciably when excess salt is added.

This data shows that polarizability can have an important effect on ion partitioning. The neutral non-polarizable domains display no favorable enthalpic interactions with the charged ions, and thus salt is expelled from the interior of the condensate. As excess salt is introduced, the osmotic pressure resulting from the supernatant concentration pushes it into the interior of the condensate. However, when the neutral blocks are polarizable, there are favorable interactions between the induced dipoles and ions. Thus the neutral blocks become less effective at expelling the salt from the condensate, consistent with the expected improved solubility of ions into polar domains[44,46,70].

Next, we analyze how ions distribute themselves between the charged and neutral domains of the coacervates. The ratio of ionic concentration in the charged to neutral domains is plotted as a function of excess salt for the chains with different charge fractions in Figure 8. Figure 8 (middle) shows the data corresponding to coacervates with non-polarizable neutral blocks. In this case, the ratio of salt concentrations in the charged to neutral domains is inversely proportional to the fraction of charged residues on the constituent chains. This ratio is ~ 1.8 for the smallest charge fraction and decreases to ~ 1 for the sequences with $N_c = 20$. This is consistent with the expectation that charged domains draw ions more readily than non-polarizable neutral domains. The charged domains reach high internal ion concentration even when they occupy a small overall volume fraction. When additional ions are introduced into the system, ions can no longer be added to the charged domains which are over-saturated. Thus the excess ions begin to enter into the neutral regions instead. Consistent with that assumption, for all values of N_c studied the relative concentration of ions between the charged and neutral domains approaches ~ 1 as the amount of excess salt increases. This situation

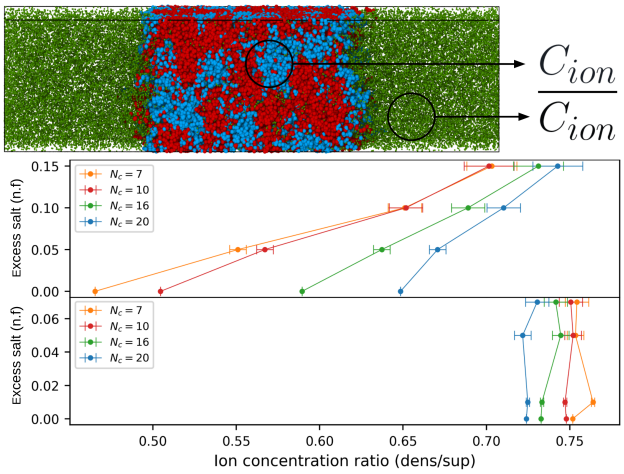

Figure 7 Changes in the ratio of ion concentrations in the coacervate and the supernatant for triblock copolymers with variable charge fraction and neutral block polarizability as a function of excess salt. (Top) A rendered image of the system and corresponding ion concentrations. Charged monomers shown in red, neutral monomers in blue, and ions in green. Solvent hidden for clarity. (Middle) Plot of the relative concentration of ions in the condensed and the dilute phase as a function of excess salt for the coacervates with the non-polarizable neutral blocks and (bottom) with the polarizable neutral blocks. n.f. stands for number fraction.

changes when the neutral block is polarizable. In this case, the relative concentrations of ions between the charged and neutral domains are almost independent of N_c and all ~ 1 . This effect is a combination of the weak compressibility and electrostatics. As the ions cannot be accommodated in the tightly-packed charged-polarizable domains, they preferentially migrate to the more dilute neutral domains, which now, due to the induced dipoles, display favorable electrostatic interactions with the charged ions.

3.5 Microstructure

Finally, we take a closer look into the microstructure present in the coacervates made of triblock polymer chains with variable N_c and different combinations of block polarizabilities, Figure 2 b). In the top panel of Figure 6 under conditions of no excess salt, we observed structures suggestive of the formation of lamellar domains. In the systems simulating coexistence between the polymer-rich phase and the supernatant, any ordered structure could potentially be frustrated by the small box cross-section and interfaces with the supernatant. To test whether our systems would form ordered microstructures, we extract the number fractions of species present in the polymer-rich phase in the long simulation boxes and use them to initialize simulations in a bigger $(50 \times 50 \times 75)$ box. We investigate how microstructure changes as a function of N_c and different combinations of polarization on the charged and uncharged blocks. These simulations are begun from random configurations and subsequently run for tens of polymer diffusion times to allow for the formation of microstructure.

While we commonly found that the charged domains aggregated together within the polymer-rich phases, ordered domains were only observed in a few specific cases. Figure 9 shows typical morphologies of disordered systems with polarizable neutral

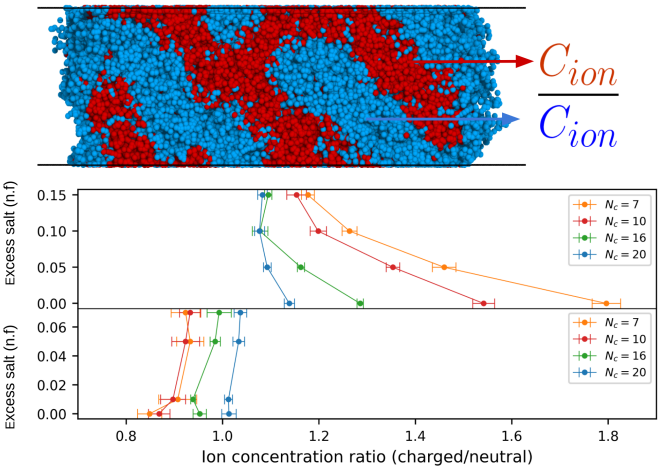

Figure 8 Salt partitioning between different domains of the coacervate. a) A rendered image of the system and corresponding ion concentrations, color scheme is the same as Figure 7. b) and c) Changes in partitioning within the domains of coacervates with non-polarizable (b) and polarizable (c) neutral blocks as a function of excess salt. n.f. stands for number fraction.

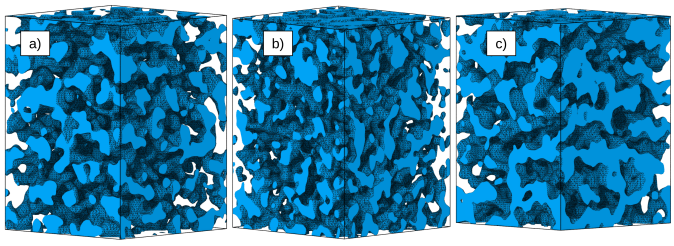

Figure 9 Lack of ordered microstructure in coacervates with polarizable neutral block. Figure only shows the boundaries of the charged regions in the coacervates with $N_c = 10$ (a), $N_c = 16$ (b), and $N_c = 20$ (c). All simulations are performed in a $50 \times 50 \times 75$ box, and the value of χ is fixed at 1.5. The surfaces correspond to approximately constant density values taken at half of the average polymer density and were rendered in OVITO Pro[71].

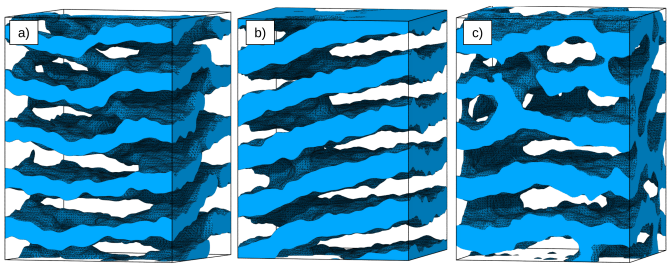

Figure 10 Microstructure developed in the solutions of triblock chains with $\chi = 0.7$ with non-polarizable neutral blocks and polarizable charged blocks. Surfaces depict the boundaries of the charged domains of coacervates with $N_c = 10$ (a), $N_c = 16$ (b), and $N_c = 20$ (c). In all cases, lamellar microstructure is observed, with different level of defectiveness. All simulations are performed in a $50 \times 50 \times 75$ box. No lamellae observed when the charged blocks are non-polarizable.

blocks. The defining distinction between the charged and uncharged blocks is the presence of electrostatic attraction in the first case, and its lack in the later case. However, when induced dipoles are added to the neutral block, the uncharged monomers can now attract the monomers on the charged blocks. This leads to a relatively weak repulsion between the blocks and no long-range ordering. We next consider systems with non-polarizable neutral blocks and perform simulations at three values of χ, 0.7, 0.9 and 1.5. When the charged block is polarizable, the polymer-rich phase develops lamellar microstructure for N_c values of 10, 16, and 20, for all values of χ studied. A few residual defects connecting some of the layers are present. This range of N_c corresponds to the charge-fraction range of $f_c = 2N_c/N \in [0.22, 0.53]$. The final morphologies at $\chi = 0.7$ for the systems which create lamellae are shown in Figure 10. When charged blocks are non-polarizable, no lamellae are observed. Structure factor analysis reports $q^* \approx 0.42$ for all three coacervates, corresponding to the equilibrium spacing between lamellae of $d \approx 15.0$.

To our knowledge, no experimental or theoretical study has been done on systems that would exactly correspond to ours, which would allow a direct comparison. However, we can still compare our results to the results obtained for the work on similar systems. For example, our observations are consistent with the theoretical study of the isolated neutral ABA triblock polymer blends[72]. Consistent with the theoretical predictions for the terminal block lengths of $N_c = 25$ and 7 (corresponding to $f_c = 0.67$ and 19, respectively), we do not observe any long-range order in our system, while within the $f_c \in [0.22, 0.53]$ range we observe lamellae. Microstructure corresponding to $N_c = 25$ is shown in Figure 11. Although the charged domains adopt elongated structures, no long-range order or hexagonal packing as expected of an ordered cylindrical phase is observed. The differences between our results and the theoretical prediction for the simple ABA polymer blend likely come from the presence of the electrostatic interactions in our systems, along with the explicit polarizable solvent and ions. In addition, our systems display some similarity to the behaviour of the traditional block copolymer solution phase diagrams[73].

Since all our simulations involve explicit counterions, we investigate how their presence affects the microstructure. The ion

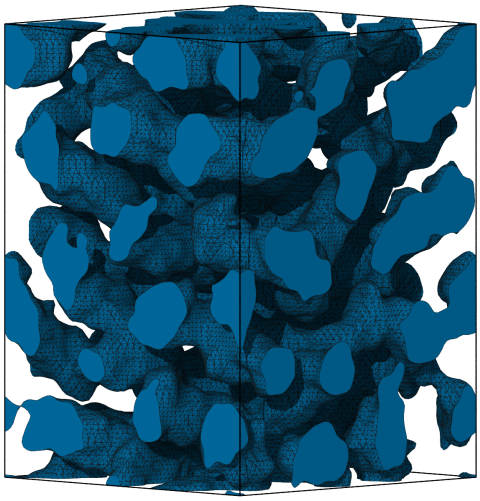

Figure 11 Microstructure developed in the coacervate of triblock with $N_c = 25$, polarizable charged blocks, non-polarizable neutral blocks, and $\chi = 1.0$. Figure only shows the neutral regions of the condensate.

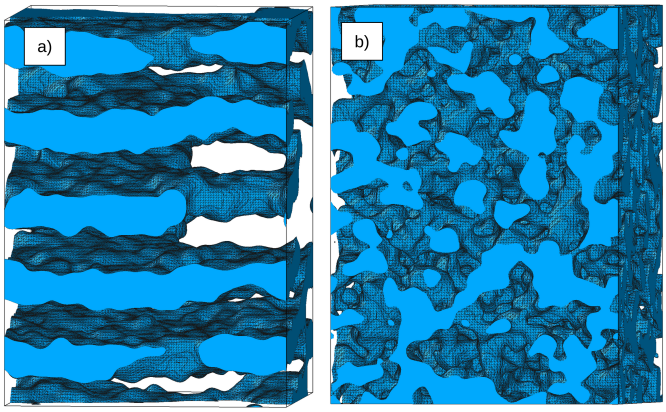

Figure 12 Effect of ion concentration on the microstructure developed in the coacervate of triblock with $N_c = 16$, non-polarizable charged blocks, non-polarizable neutral block, and $\chi = 1.0$. System without any ions present (a), and the system where each charged monomer has a corresponding counterion (b). Surfaces correspond to the boundaries of the charged regions of the condensate.

concentrations in the systems corresponding to the results shown in Figures 9, 10 and 11 correspond to $\sim 60\%$ of the values found in the long simulation boxes, where each charged monomer has a corresponding counterion. To test the effect of salt concentration on the microstructure, we initialize a set of new simulations in the $50 \times 50 \times 75$ box containing only the polymer-rich phase. These systems contain either no ions (no salt), or have the ionic concentration corresponding to that found in the long boxes (full salt) with each charged monomer having its corresponding counterion. We again test all the polarizability combinations, for simplicity keeping $\chi = 1.0$. As previously, only disordered microstructure is observed for the case of polarizable natural blocks, regardless of the amount of ions. When no ions are present in the system, chains with $N_c = 10$, 16 and 20 again form lamellae, but this time this occurs both for the case of polarizable and non-polarizable charged blocks. When counterions are introduced at the "full salt" concentration, lamellae persist in the systems with polarizable charged blocks but they disappear when charged domains are non-polarizable, Figure 12 b). The results with the non-polarizable neutral block and non-polarizable charged blocks are shown in Figure 12 for the selected case of $N_c = 16$.

Non-polarizable charged monomers have a weaker affinity to each other as compared with their polar counterparts. The inclusion of ions screens the electrostatic interactions and partially neutralizes the charge. When the charged blocks are non-polar, there is no dielectric mismatch between the charged and neutral blocks, and the addition of neutralizing ions increases the miscibility of these domains. This causes the lamellar microstructure to disappear.

4 Conclusions

In this work, we investigated the effect of monomer polarizability on the properties of the condensates formed by the polymers with a variable charge fraction. We performed coarse-grained simulations using the TILD method, modeling the polymers as discrete Gaussian chains. All simulations included explicit solvent and counterions. Consistent with the results from the previous theoretical studies, we demonstrated that variations in monomer polarizability and the dielectric constant of the solvent exert only a minor effect on the bulk properties of the condensates. However, we found that polarizability can have a significant effect both on the partitioning of salt ions and the microstructure of the condensate. Specifically, our data demonstrated that polar-charged monomers create higher density domains than their non-polar counterparts, due to additional "van der Waals-like" interactions of their dipoles. In comparison, placing induced dipoles on neutral monomers reduces the density of their condensates. In terms of ion partitioning, we showed that the nature of the neutral block has a significant effect on this phenomenon. When the neutral monomers are non-polarizable, they expel ions from their domains, which then migrate into the charged domains. However, when neutral monomers carry induced dipoles, the ions preferentially partition to the neutral domains. Finally, we demonstrated that the microstructure within the condensates depends both on the charge fraction of the polymer chains, and the polarizability of the charged and neutral blocks. Non-polarizable blocks do not mix with charged regions, which is essential for the ordered microstructure to develop. When neutral blocks are polarizable, the miscibility with charged blocks increases, and no long-range order can develop.

Our study can serve as an entry point for a more detailed investigation concerned with the phenomenon of LLPS. Our results demonstrated general trends and provided clues about the nature of the forces which modulate the propensity of polymer solutions to undergo LLPS. Future research can focus on real polymer chains or polypeptide sequences. Monomer polarizability and solvent dielectric constant can be tuned to match the experimental values associated with the system of interest, and these details have rarely been considered in previous work. Reducing the level of coarse-graining would enable future studies to resolve microscopic interactions between the monomer and the

solvent that emerge due to the induced dipoles. In addition, this work is relevant to biological studies, as the region studied also encompassed the low-χ regime. This corresponds to the weak association regime found *in vivo* in the interactions between the biomolecules. We believe that understanding the factors which modulate LLPS will be an essential step in harnessing this process to aid in pharmaceutical and clinical applications. It will also provide a better understanding on how LLPS helps maintain cellular homeostasis, what causes its deregulation, and how to control this process *in vivo*.

The recent use coarse-grained models with explicit polarizability in simulating biocondensates underscores the importance and applicability of our approach. Low resolution models with classical dipoles have been successfully applied to study protein misfolding and aggregation[74], and interactions of lipids with polypeptides[75]. We believe that our approach can be used to study these systems in a computationally efficient manner, and future work could extract properties of the polymer-rich phases (such as the rheology or dielectric properties) to compare to experiments.

Author Contributions

ZMJ: Investigation, Formal Analysis, Methodology, Software, Resources, Writing – Original Draft, Writing – Review & Editing, Visualization;
RAR: Conceptualization, Supervision, Methodology, Writing – Review & Editing, Software, Resources;

Conflicts of interest

There are no conflicts to declare.

Acknowledgements

This work used Bridges-2 GPU at Pittsburgh Supercomputing Center through allocations DMR150034 and CHM220015 from the Advanced Cyberinfrastructure Coordination Ecosystem: Services & Support (ACCESS) program, which is supported by National Science Foundation grants #2138259, #2138286, #2138307, #2137603, and #2138296. This work was supported by the National Science Foundation through grant MRSEC/DMR-1720530, partially supported by NSF CHE-2203905, and the Department of Physics and Astronomy at the University of Pennsylvania. Simulations were performed using MATILDA.FT[56]. Part of the data analysis and generation of images for the publication was done using OVITO Pro[71].

Notes and references

1 C. E. Sing and S. L. Perry, *Soft Matter*, 2020, **16**, 2885–2914.
2 S. L. Perry and C. E. Sing, *Macromolecules*, 2015, **48**, 5040–5053.
3 J. Qin, D. Priftis, R. Farina, S. L. Perry, L. Leon, J. Whitmer, K. Hoffmann, M. Tirrell and J. J. de Pablo, *ACS Macro Letters*, 2014, **3**, 565–568.
4 S. E. Herrera, M. L. Agazzi, E. Apuzzo, M. L. Cortez, W. A. Marmisollé, M. Tagliazucchi and O. Azzaroni, *Soft Matter*, 2023, **19**, 2013–2041.
5 S. M. Lalwani, C. I. Eneh and J. L. Lutkenhaus, *Physical Chemistry Chemical Physics*, 2020, **22**, 24157–24177.
6 B. S. Schuster, G. L. Dignon, W. S. Tang, F. M. Kelley, A. K. Ranganath, C. N. Jahnke, A. G. Simpkins, R. M. Regy, D. A. Hammer, M. C. Good and J. Mittal, *Proceedings of the National Academy of Sciences*, 2020, **117**, 11421–11431.
7 S. L. Perry, *Current Opinion in Colloid & Interface Science*, 2019, **39**, 86–97.
8 G. Krainer, T. J. Welsh, J. A. Joseph, J. R. Espinosa, S. Wittmann, E. de Csilléry, A. Sridhar, Z. Toprakcioglu, G. Gudiškytė, M. A. Czekalska, W. E. Arter, J. Guillén-Boixet, T. M. Franzmann, S. Qamar, P. S. George-Hyslop, A. A. Hyman, R. Collepardo-Guevara, S. Alberti and T. P. J. Knowles, *Nature Communications*, 2021, **12**, 1085.
9 M. Abbas, W. P. Lipiński, J. Wang and E. Spruijt, *Chemical Society Reviews*, 2021, **50**, 3690–3705.
10 S. F. Banani, H. O. Lee, A. A. Hyman and M. K. Rosen, *Nature Reviews Molecular Cell Biology*, 2017, **18**, 285–298.
11 Y. Shin and C. P. Brangwynne, *Science*, 2017, **357**, eaaf4382.
12 D. M. Mitrea and R. W. Kriwacki, *Cell Communication and Signaling*, 2016, **14**, 1.
13 D. Berchtold, N. Battich and L. Pelkmans, *Molecular Cell*, 2018, **72**, 1035–1049.e5.
14 M. Zeng, Y. Shang, Y. Araki, T. Guo, R. L. Huganir and M. Zhang, *Cell*, 2016, **166**, 1163–1175.e12.
15 A. H. S. Martinelli, F. C. Lopes, E. B. O. John, C. R. Carlini and R. Ligabue-Braun, *International Journal of Molecular Sciences*, 2019, **20**, 1322.
16 N. M. Kanaan, C. Hamel, T. Grabinski and B. Combs, *Nature Communications*, 2020, **11**, 2809.
17 J. Lu, J. Qian, Z. Xu, S. Yin, L. Zhou, S. Zheng and W. Zhang, *Frontiers in Cell and Developmental Biology*, 2021, **9**, 631486.
18 X. Tong, R. Tang, J. Xu, W. Wang, Y. Zhao, X. Yu and S. Shi, *Signal Transduction and Targeted Therapy*, 2022, **7**, 221.
19 A. S. Indulkar, Y. Gao, S. A. Raina, G. G. Z. Zhang and L. S. Taylor, *Molecular Pharmaceutics*, 2016, **13**, 2059–2069.
20 P. Zhao, W. Han, Y. Shu, M. Li, Y. Sun, X. Sui, B. Liu, B. Tian, Y. Liu and Q. Fu, *Journal of Controlled Release*, 2023, **353**, 42–50.
21 L. S. Taylor and G. G. Zhang, *Advanced Drug Delivery Reviews*, 2016, **101**, 122–142.
22 R. J. Wheeler, *Emerging Topics in Life Sciences*, 2020, **4**, 331–342.
23 B. A. Conti and M. Oppikofer, *Trends in Pharmacological Sciences*, 2022, **43**, 820–837.
24 A. M. Rumyantsev, N. E. Jackson and J. J. de Pablo, *Annual Review of Condensed Matter Physics*, 2021, **12**, 155–176.
25 A. B. Kayitmazer, *Advances in Colloid and Interface Science*, 2017, **239**, 169–177.
26 C. E. Sing, *Advances in Colloid and Interface Science*, 2017, **239**, 2–16.
27 A. Veis, *Advances in Colloid and Interface Science*, 2011, **167**, 2–11.
28 C. E. Sing and S. L. Perry, *Soft Matter*, 2020, **16**, 2885–2914.

29 R. Das and R. Pappu, *Proceedings of the National Academy of Sciences of the United States of America*, 2013, **110**, 13392–13397.

30 S. P. O. Danielsen, J. McCarty, J.-E. Shea, K. T. Delaney and G. H. Fredrickson, *Proceedings of the National Academy of Sciences*, 2019, **116**, 8224–8232.

31 S. L. Perry and C. E. Sing, *Macromolecules*, 2015, **48**, 5040–5053.

32 M. Radhakrishna, K. Basu, Y. Liu, R. Shamsi, S. L. Perry and C. E. Sing, *Macromolecules*, 2017, **50**, 3030–3037.

33 T. K. Lytle and C. E. Sing, *Soft Matter*, 2017, **13**, 7001–7012.

34 S. Adhikari, V. M. Prabhu and M. Muthukumar, *Macromolecules*, 2019, **52**, 6998–7004.

35 M. Andreev, V. M. Prabhu, J. F. Douglas, M. Tirrell and J. J. de Pablo, *Macromolecules*, 2018, **51**, 6717–6723.

36 A. M. Rumyantsev, N. E. Jackson, B. Yu, J. M. Ting, W. Chen, M. V. Tirrell and J. J. de Pablo, *ACS Macro Letters*, 2019, **8**, 1296–1302.

37 J. Qin, D. Priftis, R. Farina, S. L. Perry, L. Leon, J. Whitmer, K. Hoffmann, M. Tirrell and J. J. de Pablo, *ACS Macro Letters*, 2014, **3**, 565–568.

38 R. A. Riggleman, R. Kumar and G. H. Fredrickson, *The Journal of Chemical Physics*, 2012, **136**, 024903.

39 Y.-H. Lin, J. D. Forman-Kay and H. S. Chan, *Phys. Rev. Lett.*, 2016, **117**, 178101.

40 L. Sawle and K. Ghosh, *The Journal of Chemical Physics*, 2015, **143**, 085101.

41 A. N. Amin, Y.-H. Lin, S. Das and H. S. Chan, *The Journal of Physical Chemistry B*, 2020, **124**, 6709–6720.

42 J. Huihui and K. Ghosh, *The Journal of Chemical Physics*, 2020, **152**, 161102.

43 J. Wessén, T. Pal and H. S. Chan, *The Journal of Chemical Physics*, 2022, **156**, 194903.

44 Z.-G. Wang, *Physical Review E*, 2010, **81**, 021501.

45 J. N. Israelachvili, *Intermolecular and Surface Forces*, Elsevier, 2011.

46 K. J. Hou and J. Qin, *Macromolecules*, 2018, **51**, 7463–7475.

47 J. Wessén, T. Pal, S. Das, Y.-H. Lin and H. S. Chan, *The Journal of Physical Chemistry B*, 2021, **125**, 4337–4358.

48 P. E. M. Lopes, B. Roux and A. D. MacKerell, *Theoretical Chemistry Accounts*, 2009, **124**, 11–28.

49 C. Schröder, A. Lyons and S. W. Rick, *Physical Chemistry Chemical Physics*, 2020, **22**, 467–477.

50 F.-Y. Lin, P. E. M. Lopes, E. Harder, B. Roux and A. D. J. MacKerell, *Journal of Chemical Information and Modeling*, 2018, **58**, 993–1004.

51 V. S. Inakollu, D. P. Geerke, C. N. Rowley and H. Yu, *Current Opinion in Structural Biology*, 2020, **61**, 182–190.

52 S. Wang and N. M. Cann, High Performance Computing Systems and Applications, Berlin, Heidelberg, 2010, pp. 76–98.

53 J. A. Lemkul, J. Huang, B. Roux and A. D. MacKerell, *Chemical Reviews*, 2016, **116**, 4983–5013.

54 M. Deserno and C. Holm, *The Journal of chemical physics*, 1998, **109**, 7678–7693.

55 M. C. Villet and G. H. Fredrickson, *The Journal of Chemical Physics*, 2014, **141**, 224115.

56 Z. M. Jedlinska, C. Tabedzki, C. Gillespie, N. Hess, A. Yang and R. A. Riggleman, *The Journal of Chemical Physics*, 2023, **159**, 014108.

57 J. P. Koski, H. Chao, C. Tabedzki and R. A. Riggleman, *Theory and Modeling of Polymer Nanocomposites*, 2021, 45–79.

58 G. H. Fredrickson and K. T. Delaney, *Field-Theoretic Simulations in Soft Matter and Quantum Fluids*, Oxford University Press, 2023, vol. 173.

59 M. W. Matsen, *Journal of Physics: Condensed Matter*, 2001, **14**, R21.

60 A. Garaizar and J. R. Espinosa, *The Journal of Chemical Physics*, 2021, **155**, 125103.

61 S. P. O. Danielsen, J. McCarty, J.-E. Shea, K. T. Delaney and G. H. Fredrickson, *The Journal of Chemical Physics*, 2019, **151**, 034904.

62 P. E. M. Lopes, J. Huang, J. Shim, Y. Luo, H. Li, B. Roux and A. D. MacKerell, *Journal of Chemical Theory and Computation*, 2013, **9**, 5430–5449.

63 A. Dequidt, J. Devémy and A. A. H. Pádua, *Journal of Chemical Information and Modeling*, 2016, **56**, 260–268.

64 J. A. Lemkul, J. Huang, B. Roux and A. D. MacKerell, *Chemical Reviews*, 2016, **116**, 4983–5013.

65 E. Helfand, *The Journal of chemical physics*, 1975, **62**, 999–1005.

66 W. Zheng, G. L. Dignon, N. Jovic, X. Xu, R. M. Regy, N. L. Fawzi, Y. C. Kim, R. B. Best and J. Mittal, *The Journal of Physical Chemistry B*, 2020, **124**, 11671–11679.

67 G. L. Dignon, W. Zheng, Y. C. Kim, R. B. Best and J. Mittal, *PLOS Computational Biology*, 2018, **14**, e1005941.

68 F. Camerin, N. Gnan, L. Rovigatti and E. Zaccarelli, *Scientific Reports*, 2018, **8**, 14426.

69 C. Balzer and A. L. Frischknecht, *Macromolecules*, 2022, **55**, 9980–9989.

70 J. Lou, S. Friedowitz, J. Qin and Y. Xia, *ACS Central Science*, 2019, **5**, 549–557.

71 A. Stukowski, *Modelling and Simulation in Materials Science and Engineering*, 2009, **18**, 015012.

72 M. W. Matsen, *Macromolecules*, 2012, **45**, 2161–2165.

73 T. P. Lodge, B. Pudil and K. J. Hanley, *Macromolecules*, 2002, **35**, 4707–4717.

74 S. J. Ganesan and S. Matysiak, *Phys. Chem. Chem. Phys.*, 2016, **18**, 2449–2458.

75 S. J. Ganesan, H. Xu and S. Matysiak, *Phys. Chem. Chem. Phys.*, 2016, **18**, 17836–17850.